JASS *Journal of Astronomy and Space Sciences*

Baseline Design and Performance Analysis of Laser Altimeter for Korean Lunar Orbiter

Hyung-Chul Lim[1†], Gregory A. Neumann[2], Myeong-Hwan Choi[1], Sung-Yeol Yu[1], Seong-Cheol Bang[1], Neung-Hyun Ka[1], Jong-Uk Park[1], Man-Soo Choi[1], Eunseo Park[1]

[1]Korea Astronomy and Space Science Institute, Daejeon 34055, Korea
[2]NASA Goddard Space Flight Center, Greenbelt, MD 20771, USA

Korea's lunar exploration project includes the launching of an orbiter, a lander (including a rover), and an experimental orbiter (referred to as a lunar pathfinder). Laser altimeters have played an important scientific role in lunar, planetary, and asteroid exploration missions since their first use in 1971 onboard the Apollo 15 mission to the Moon. In this study, a laser altimeter was proposed as a scientific instrument for the Korean lunar orbiter, which will be launched by 2020, to study the global topography of the surface of the Moon and its gravitational field and to support other payloads such as a terrain mapping camera or spectral imager. This study presents the baseline design and performance model for the proposed laser altimeter. Additionally, the study discusses the expected performance based on numerical simulation results. The simulation results indicate that the design of system parameters satisfies performance requirements with respect to detection probability and range error even under unfavorable conditions.

Keywords: laser altimeter, Korean lunar orbiter, LALE, lunar topography

1. INTRODUCTION

Korea's lunar exploration project currently consists of two phases. Phase 1 includes the launch of an experimental orbiter termed as a lunar pathfinder by 2018, whereas phase 2 involves the launch of an orbiter and a lander (including a rover) by 2020. In 1971, space-borne laser altimeters were first used onboard the Apollo 15 mission to the Moon. Subsequently, these altimeters were used for many lunar, planetary, and asteroid exploration missions, as shown in Table 1. Their measurements provide powerful geophysical tools for exploring extraterrestrial objects via methods such as topography and gravity. Specifically, the lunar orbiter laser altimeter (LOLA) on the lunar reconnaissance orbiter (LRO) mission provides complete measurement data to facilitate landing-site selection for future robotic and human exploration missions and to detect the presence of water and/or ice on or near the lunar surface (Riris et al. 2010). Hence, this study proposed a laser altimeter as a scientific instrument for the Korean lunar orbiter. The proposed altimeter provides the global topography of the lunar surface and better understanding of gravitational field. Additionally, it supports other payloads such as terrain mapping camera or a spectral imager. Furthermore, it is designed to provide altimetry data even in permanently shadowed regions to derive a better understating of lunar physics.

Table 1. Space missions equipped with a laser altimeter

Target	Mission (year, nation)
Moon	Apollo 15 (1971, USA), Apollo 16 (1972, USA), Apollo 17 (1972, USA), Clementine (1994, USA), SELENE (2007, Japan), Chang'E 1 (2007, China), Chandrayaan-1 (2008, Indida), LRO (2009, USA), Chang'E 2 (2010, China)
Planet	Mars Observer (1992, USA), Mars Global Surveyor (1996, USA), MESSENGER (2004, USA), BepiColombo (2017, Europe), JUICE (2020, Europe)
Asteroid	NEAR-Shoemaker (1996, USA), Hayabusa (2003, Japan), Hayabusa-2 (2014, Japan), OSIRIS-Rex (2016, USA)

The round-trip flight time of laser pulses provides meter or even centimeter range resolution by employing short pulse lasers with widths of several nanoseconds. Laser altimetry determines the distance from the orbiter to the lunar surface by measuring the round-trip flight time of laser pulses. The vertical resolution of altimetry measurement is primarily determined by laser pulse width and the timing precision of altimeter electronics. The horizontal resolution is based on the footprint size on the surface and laser repetition rate. A laser altimeter provides measurements of the structure and reflectivity of the target surface in addition to straightforward range measurement. The received waveforms also contain important information about surface slope, roughness, and reflectivity since the reflected laser pulses are distorted or spread by physical surface characteristics within the footprint (Bufton 1989). The structural information, such as slope and roughness, are determined by analyzing the received pulse shape through analog processing or GHz bandwidth digitization. The direct measurement of the received pulse energy through a calibration of laser backscatter from different surfaces and normalization by the transmitted laser energy determines the surface reflectivity (Santovito et al. 2006).

Four figures of merit quantify laser altimeter performance, namely detection probability, false alarm probability, signal-to-noise ratio (SNR), and range error. A laser altimeter should be designed such that it has high detection probability, high SNR, low false alarm probability, and low range error. Hence, it is necessary to employ a trade-off between two probabilities that are based on detection threshold functions. With respect to a Mars orbiter laser altimeter (MOLA), a fixed detection threshold is applied for the transmitted pulse while the threshold levels of echo pulses are automatically and independently adjusted by an algorithm to maintain a false alarm rate of approximately 1 % per receiver channel (Abshire et al. 2000). When the SNR reduces, it is more likely that the receiver will miss or falsely detect the return pulse, and thus the probability of a false alarm increases. The range error also increases as the SNR decreases because statistical fluctuations distort the ideal return pulse shape and lead to a measurement error in the arrival time. Therefore, it is necessary to compensate the decrease in the signal strength due to aperture reductions by other instrument parameters such as higher laser pulse energies or lower electrical noise (Gunderson et al. 2006).

This study describes a baseline design for a laser altimeter of a Korean lunar orbiter to be launched during phase 2. The altimeter is named as a laser altimeter for lunar exploration (LALE). Additionally, a performance model is prescribed to evaluate system parameters of baseline instrument to meet performance requirements of detection probability and range errors under a harsh operation environment. Furthermore, a discussion of expected performance is presented based on numerical simulation and the results of the simulation. The simulation results indicate that the design of system parameters meets performance requirement even under harsh conditions such as daytime operation. Moreover, several errors in the performance model equations derived by Santovito et al. (2006) are addressed in this study.

2. BASELINE DESIGN OF LALE INSTRUMENT

The design of the LALE instrument follows design drivers of Korean lunar orbiter mission, such as low mass, low power demands, and high reliability in the harsh lunar environment. It is assumed that the orbiter has a circular polar orbit with an altitude ranging from 70 km to 130 km, which is the same as that of Lunar Pathfinder launched during phase 1. The performance requirements given to achieve a successful scientific mission include the following: ≥ 95 % for detection probability, ≤ 0.1 % for false alarm probability, and ≤ 5 m for range error. Hence, it is necessary to conduct a baseline design to meet these requirements within an allocated resource budget. Specifically, it is important to consider several environmental factors including solar radiation, vacuum ultraviolet irradiation, thermal vacuum, extreme temperature, plasma, and charged particle radiation to ensure system performance (Wang et al. 2010).

Fig. 1 shows the functional block diagram of LALE, which involves use of physical properties to identify three units, namely a transmitter unit, a receiver unit, and an electronics unit. The electronics unit comprises analog electronics and a digital processing unit that consists of instrument control electronics and range measurement electronics. The transmitter uses a Q-switched diode-pumped Nd:YAG laser with 1,064 nm wavelength, 3.5 mJ pulse energy, and a pulse width of 7 ns. The beam divergence of the transmitter is 0.1 mrad as measured using a Galilean beam expander that generates a lunar surface spot size of 10 m at a nominal orbit with an altitude of 100 km. A nominal ranging repetition rate of 20 Hz is used to increase the horizontal resolution along the track direction. Return laser pulses or echo pulses are focused on a silicon avalanched photo-diode (Si APD) hybrid detector through a telescope and aft optics. The telescope diameter is 140 mm with 0.4 mrad field-of-view (FOV). The aft optics behind the telescope consists of a collimating lens, an optical band-pass filter, and a focusing lens, which is designed to minimize the background noise from solar radiation.
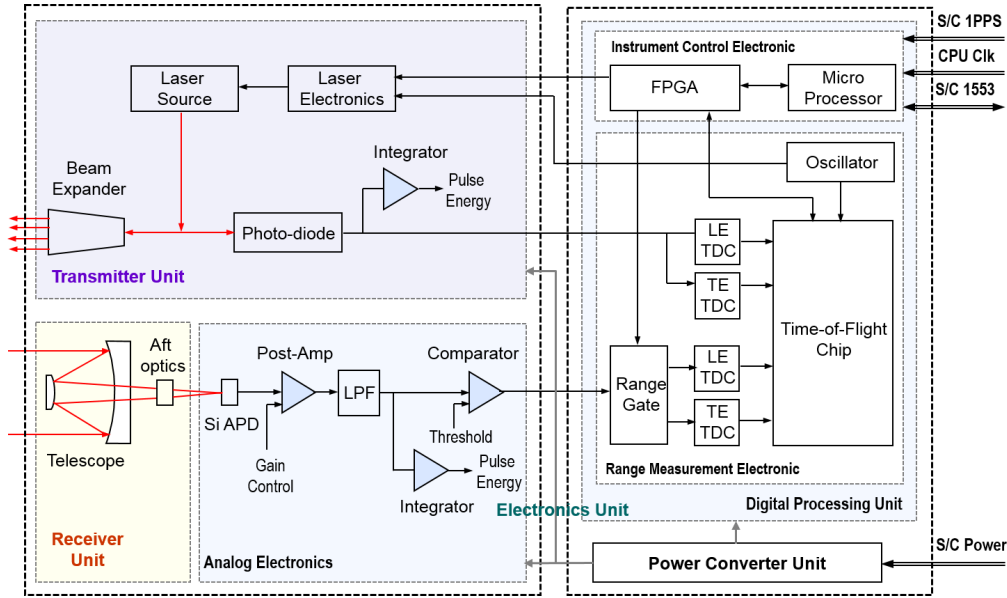
Fig. 1. LALE functional block diagram.

The purpose of analog electronics includes converting the return laser pulse from the lunar surface into a digital stop pulse to measure time-of-flight (TOF). A C30659-1-60-R8B package is considered for a Si APD detector because it was used for many space lidar instruments such as MOLA, which is commercially available and manufactured by Perkin-Elmer. The package consists of a C30954E Si APD and a very low noise GaAs FET preamplifier (1.7 pA/Hz$^{1/2}$ at 200 MHz bandwidth) (Thomas et al. 2007). Variable amplification in the post-amp (Post Amplifier) behind the Si APD hybrid detector is also performed by a gain control. It is necessary to design the amplifier bandwidth in a manner equivalent to the Si APD detector (Wang et al. 2010) to obtain excellent SNR. A low-pass filter (LPF) is used to maximize the signal detection probability, to integrate return pulses that are spread and dilated due to the lunar surface, and to achieve the reliable triggering of a comparator circuit. A comparator determines whether or not an input pulse generates a digital stop pulse based on threshold levels that are adjusted automatically to maintain a false alarm probability given by performance requirements.

A range gate is used to reduce a false alarm probability from background noise, which allows the digital pulse to pass to a time-to-digital converter (TDC) during a time interval over which the return pulse is expected to arrive. The transmitted pulse is time-stamped for a leading-edge (LE) and trailing-edge (TE) of the return pulse via an inverter in the TDC. Two LE pulses from a photo-diode in the transmitter unit and range gate provide the range measurement. The spread and dilated pulse width is computed by the difference between the LE measurement and TE measurement. Digital logic circuits including range gate generation, electronics control, and interfaces are implemented in a field-programmable gate array (FPGA). Table 2 shows the main feature of the altimeter used in the present study along with lunar laser altimeters used by previous studies to facilitate comparison at a glance. Table 3 provides the detailed specification of the altimeter. Additionally, Fig. 2 shows the three-dimensional shape obtained by LALE baseline design.

3. PERFORMANCE MODEL

3.1 Signal and Noise

The number of return photons of a laser pulse reflected by the lunar surface is influenced by the distance to the surface, surface albedo, and the design parameters of the laser altimeter. Given the assumption that the lunar surface is a diffused Lambertian target, the average number of signal photons per pulse is derived from a radar link equation as follows:

$$\bar{n}_s = \frac{E_T}{h\nu} \frac{\rho}{\pi} \frac{A_R}{R^2} T_A^2 \eta_T \, \eta_R \, \eta_F \, \eta_Q \tag{1}$$

where E_T denotes the transmitted laser pulse energy, $h\nu$ denotes the photon energy at laser wavelength, h_ν denotes surface albedo, ρ denotes the effective area of the receiving telescope, A_R denotes the range to the surface, R denotes the one-way atmospheric transmittance, T_A denotes the

Table 2. Main features of lunar laser altimeters used in previous missions including those of LALE

Instrument	LIDAR	LALT	LAM-1/2	LLRI	LOLA	LALE
Spacecraft						
Mission	Clementine	SELENE	Chang'E-1/2	Chandrayaan-1	LRO	N/A
Launch date	1994	2007	2007/2010	2008	2009	2020
Orbit altitude	400-8,300 km	100 km	200/100 km	100 km	30–200 km	70-130 km
Laser transmitter						
Laser type	Cr:Nd:YAG	Nd:YAG	Nd:YAG	Nd:YAG	Nd:YAG	Nd:YAG
Wavelength	1,064 nm	1,064 nm	1,064 nm	1,064 nm	1,064 nm	1,064 nm
Pulse energy	171 mJ	100 mJ	150 mJ	12 mJ	2.7 mJ	3.5 mJ
Pulse width	4.2 ns	17 ns	7 ns	2 ns	6 ns	7 ns
Repetition rate	0.6 Hz	1 Hz	1 Hz	10 Hz	28 Hz	20 Hz
Beam divergence	250 μrad	400 μrad	500 μrad	324 μrad	100 μrad	100 μrad
Receiver optics						
Telescope diameter	13 cm	10 cm	14 cm	20 cm	15 cm	14 cm
Field of View	500 μrad	1,000 μrad	324 μrad	890 μrad	400 μrad	400 μrad
Detector type	Si APD	Si APD	Si APD	Si APD	Si APD	Si APD
Budget						
Power	6.8 W	44.2 W	35 W	25 W	34 W	< 20 W
Mass	2.37 kg	19.09 kg	15.5 kg	10 kg	12.6 kg	< 8 kg

Table 3. Detailed specifications of the LALE

Unit	Parameter	Value
Transmitter	Optical efficiency	0.8
Receiver	Optical efficiency	0.7
	Filter transmittance	0.7
	Filter bandpass	0.4 ns
Electronics	Quantum efficiency	0.38
	APD gain	100
	Ionization coefficient ratio	0.008
	Surface dark current	20 nA
	Bulk dark current	50 pA
	Pre-amplifier noise current	1.7 pA/Hz$^{1/2}$

efficiency of the transmitting optical system, η_T denotes the efficiency of the receiving optical system, η_R denotes the interference filter transmittance, and η_F denotes the APD quantum efficiency. With respect to the lunar laser altimeter, atmospheric transmittance is neglected, i.e., T_A=1 since there is no atmosphere on the Moon.

The background noise from lunar blackbody radiation is negligible because the maximum temperature on the surface of the Moon is low (approximately 400 K) even during daytime. Thus, the average number of noise photons due to solar background and APD dark current is given by the following noise model (Santovito et al. 2006):

$$\bar{n}_b = \left(\frac{I_{Sun}}{h\nu} \rho \, A_R \left(\frac{\theta_{FOV}}{2} \right)^2 \eta_R \eta_F \eta_Q \Delta\lambda_f + \frac{I_D}{q} \right)\tau \quad (2)$$

where I_{Sun} denotes the solar spectral irradiance, θ_{FOV} denotes the receiver field of view in full angle, $\Delta\lambda_f$ denotes the interference filter bandpass, I_D denotes the Si APD dark current, τ denotes the response width of low-pass filter, and q denotes the electron charge.
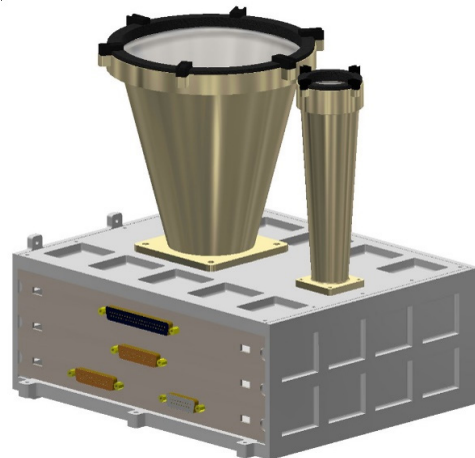
Fig. 2. Three-dimensional shape of the LALE instrument.

3.2 APD Output Statistics

With respect to an APD detector, primary photoelectrons are generated when photons are absorbed, and this is followed by the occurrence of an avalanche multiplication process by a chain of impact ionization. Given that specular reflections are not taken into account, the number of primary photoelectrons that obeys the Poisson distribution with a conditional probability density function is given below:

$$p(n \mid \bar{n}) = \frac{\bar{n}^n}{n!} e^{-\bar{n}} \quad (3)$$

where $\bar{n}$ denotes the average number of input photons and n denotes the number of primary photoelectrons. The avalanche multiplication process was studied by two previous

researches (Conradi 1972; McIntyre 1972). The conditional probability density function wherein the multiplied output of m secondary photoelectrons is generated in response to primary photoelectrons is given by the following expression:

$$p(m \mid n) = \frac{n\Gamma\left(\frac{m}{1-k}+1\right)}{m(m-n)!\Gamma\left(\frac{km}{1-k}+n+1\right)}$$
$$\times \left(\frac{1+k(G-1)}{G}\right)^{n+\frac{km}{1-k}} \times \left(\frac{(1-k)(G-1)}{G}\right)^{m-n} \quad (4)$$

where G denotes the average APD gain, k denotes the ionization coefficient ratio, and $\Gamma(\cdot)$ denotes the Gamma function. Eqs. (3) and (4) are combined, and the conditional probability density function generating electrons in the APD detector is given by the following equation:

$$p(m \mid \bar{n}) = \sum_{n=1}^{m} p(m \mid n)\frac{\bar{n}^{n}}{n!}e^{-\bar{n}}, \quad m \geq 1 \quad (5)$$

Eq. (5) is termed as an exact distribution or the McIntyre model. However, its disadvantages include the excessive amounts of computation time required in the numerical calculations of detection probabilities and false alarms arising due to the summation of large m values. A simple expression for Eq. (5) was derived with reasonable accuracy by Webb et al. (1974) as follows:

$$p(m \mid \bar{n}) = \frac{1}{\sqrt{2\pi \bar{n}G^{2}F}\left(1+\frac{m-\bar{n}G}{\bar{n}GF/(F-1)}\right)^{3/2}}$$
$$\times \exp\left(-\frac{(m-\bar{n}G)^{2}}{2\bar{n}G^{2}F\left(1+\frac{m-\bar{n}G}{\bar{n}GF/(F-1)}\right)}\right) \quad (6)$$

where F denotes an excess noise factor defined as $F = kG + (2-1/G)(1-k)$. With respect to Eq. (6), an approximation form or Webb model is preferred because of a simpler expression and shorter computation time when compared with that of the McIntyre model.

The probability density function of the APD output charge that describes the random variable x for primary photons $\bar{n}$ over the integration interval can be written as follows (Sun et al. 1992):

$$p(x \mid \bar{n}) = \sum_{m=0}^{\infty} p(x \mid m)p(m \mid \bar{n}) \quad (7)$$

where $p(x|m)$ is also termed as the conditional probability density function of circuit noise, which is considered as a Gaussian distribution because circuit noises, such as pre-amplifier and surface leakage current, constitute Gaussian

random variables as given below:

$$p(x \mid m) = \frac{1}{\sqrt{2\pi\sigma_{c}^{2}}}\exp\left(-\frac{(x-\bar{x}_{m})^{2}}{2\sigma_{c}^{2}}\right) \quad (8)$$

with mean and variance given by the previous study (Santovito et al. 2006) as follows:

$$\bar{x}_{m} = m + \frac{I_{DS}\tau}{qG}, \quad \sigma_{c}^{2} = \frac{I_{A}^{2}\tau}{q^{2}} + \frac{I_{DS}\tau}{qG}$$

where I_{DS} denotes the surface leakage current and I_{A} denotes the preamplifier noise current. The APD dark current generally consists of two components, namely surface leakage current and bulk leakage current (I_{DB}). The surface leakage current does not trigger avalanche events because it is not multiplied by APD internal gain, but it behaves like a constant DC current. In contrast, the bulk leakage current undergoes an avalanche multiplication process and behaves like a source of background radiation noise (Sun et al. 1992). Thus, the total APD dark current is given by the following expression:

$$I_{D} = I_{DS} + I_{DB}G \quad (9)$$

3.3 Probabilities of Detection and False Alarm

Typically, the optimization of laser altimeter performance involves a trade-off between detection and false alarm probabilities. Hence, it is necessary to study the relationship between two probabilities as a function of the detection threshold levels. False alarm probability due to background noise refers to the probability that the receiver noise exceeds the threshold level and provides false TOF measurement. The distribution of secondary photoelectrons m is assumed to be continuous and Gaussian. Using Eqs. (5), (7), and (8), false alarm probability (P_{FA}) and detection probability (P_{D}) are given by the following expressions:

$$P_{D} = \int_{x_{th}}^{\infty} p(x \mid \bar{n}_{sb} = \bar{n}_{s} + \bar{n}_{b})dx = \frac{1}{2}\int_{0}^{\infty} p(m \mid \bar{n}_{sb}) \, \text{erfc}\left(\frac{(x_{th}-\bar{x}_{m})}{\sqrt{2}\sigma_{c}}\right)dm \quad (10)$$

$$P_{FA} = \int_{x_{th}}^{\infty} p(x \mid \bar{n}_{b})dx = \frac{1}{2}\int_{0}^{\infty} p(m \mid \bar{n}_{b}) \, \text{erfc}\left(\frac{(x_{th}-\bar{x}_{m})}{\sqrt{2}\sigma_{c}}\right)dm \quad (11)$$

where erfc$(\cdot)$ denotes the complementary error function defined as follows:

$$\text{erfc}(x_{th}) = \frac{2}{\sqrt{\pi}}\int_{x_{th}}^{\infty} e^{-x^{2}}dx$$

The McIntyre or Webb models can be used as the conditional probability density function, denoted by $p(m|\bar{n})$ in Eq. (10). If an approximation expression such as the Webb model is used, a new variable $z = (m-\bar{n}G)/\sqrt{\bar{n}G^{2}F}$ in $p(m|\bar{n})$ can be introduced in the Webb model, and thus false

alarm and detection probabilities are given by the following expressions:

$$P_D = \frac{\sigma_{sb}}{2} \int_{-n_{sb}G/\sigma_{sb}}^{+\infty} p(z \mid n_{sb}) dz \, \mathrm{erfc}\left(\frac{x_{th} - \sigma_{sb}z - n_{sb}G - I_{DS}\tau/qG}{\sqrt{2}\sigma_c} \right) \quad (12)$$

$$P_{FA} = \frac{\sigma_b}{2} \int_{-n_bG/\sigma_b}^{+\infty} p(z \mid n_b) dz \, \mathrm{erfc}\left(\frac{x_{th} - \sigma_b z - n_b G - I_{DS}\tau/qG}{\sqrt{2}\sigma_c} \right) \quad (13)$$

where

$$\sigma_{sb} = \sqrt{\bar{n}_{sb}G^2 F}$$

$$p(z \mid n_{sb}) = \frac{1}{\sqrt{2\pi}\sigma_{sb}\left(1 + \frac{G(F-1)z}{\sigma_{sb}}\right)^{3/2}} \times \exp\left(-\frac{z^2}{2\left(1 + \frac{G(F-1)z}{\sigma_{sb}}\right)}\right)$$

and

$$\sigma_b = \sqrt{\bar{n}_b G^2 F}$$

$$p(z \mid n_b) = \frac{1}{\sqrt{2\pi}\sigma_b\left(1 + \frac{G(F-1)z}{\sigma_b}\right)^{3/2}} \times \exp\left(-\frac{z^2}{2\left(1 + \frac{G(F-1)z}{\sigma_b}\right)}\right)$$

By comparing Eqs. (10)-(13) to the equations derived by Santovito et al. (2006), several errors in Eqs. (13), (15) and (16) of the extant research are revealed.

3.4 Signal-to-Noise Ratio and Range Error

There are several noise sources such as shot noise, background noise, detector dark current, and pre-amplifier noise. In this study, echo or return pulse width in the SNR equation (Burns et al. 1991) is considered because the transmitted laser pulse is spread out and dilated. Thus, the modified SNR equation is given by the following expression:

$$SNR = \frac{i_S^2}{i_N^2} = \frac{i_S^2}{i_{NS}^2 + i_{NB}^2 + i_{ND}^2 + i_{NA}^2} \quad (14)$$

$$= \frac{(q\bar{n}_s/\sigma_p)^2 R_0^2 G^2}{\left[2qR_0 G^2 F(qn_s/\sigma_p + q\bar{n}_b) + 2q(I_{DS} + I_{DB}G^2 F) + I_{NA}^2\right]B}$$

where i_s denotes the signal current and i_N denotes the noise current by shot noise (i_{NS}), background noise (i_{NB}), dark current noise (i_{ND}), and pre-amplifier noise (i_{NA}). Furthermore, σ_p represents the echo pulse width, R_0 represents the unity gain responsivity that includes a general definition of $q\eta_Q/hv$, I_{NA} represents pre-amplifier input noise current, and B represents the detection bandwidth computed by $1/3\tau$ (Abshire et al. 2000; Santovito et al. 2006). Shot noise or quantum noise

is time-dependent on fluctuations in APD detector output caused by the random arrival of signal photons.

Ranging precision for single-shot measurement is inversely proportional to the square of SNR due to the timing uncertainty that results from signal amplitude variation with a fixed threshold level (Bufton 1989). The RMS (root mean square) range error is given by the following equation:

$$\Delta R = \frac{c\sigma_p}{2\sqrt{SNR}} \quad (15)$$

where c denotes the speed of light in vacuum. An error is also found in the Eq. (23) of range error equation given by Santovito et al. (2006).

3.5 Echo Pulse Width

The echo pulse width is used to estimate the surface slope and roughness because the echo waveform is distorted by physical surface characteristics within the laser footprint. Additionally, it is related to the range error as shown in Eq. (15) since the measurement epoch of the leading edge or trailing edge is dependent on the echo waveform. An analytic expression for the mean-square echo pulse width is given by the following expression (Gardner 1992):

$$\sigma_p^2 = \left(\sigma_l^2 + \sigma_h^2\right) + \frac{4\mathrm{Var}(\Delta\xi)\cos^2 S_\parallel}{c^2 \cos^2(\phi + S_\parallel)}$$

$$+ \frac{4z^2 \tan^2(\theta_T/2)}{c^2 \cos^2\phi}\left[\tan^2(\theta_T/2) + \tan^2(\phi + S_\parallel) + \frac{\tan^2 S_\perp \cos^2 S_\parallel}{\cos^2(\phi + S_\parallel)}\right] \quad (16)$$

where σ_l denotes the RMS laser pulse width, σ_h denotes the RMS width of the receiver impulse response, $\Delta\xi$ denotes the surface roughness, ϕ denotes the nadir angle of laser beam, and θ_T denotes the laser beam divergence in full angle. Furthermore, S denotes the surface slope that consists of two components, namely a surface slope parallel to the nadir direction ($S_\parallel$) and a surface slope normal to nadir direction ($S_\perp$). The first term in Eq. (16) accounts for system effects and the second term accounts for roughness effects. The third term corresponds to the beam curvature, nadir angle, and slope effects. The RMS width of the receiver impulse width is related to low-pass filter impulse width (Abshire et al. 2000) as follows: $\sigma_h = \left(\tau/2\sqrt{2\ln 2}\right)$.

4. SIMULATION RESULTS AND DISCUSSION

In order to satisfy scientific requirements, it is necessary to determine several design parameters. However, a trade-off between these parameters is essential due to the allocated resource budget. Specific system specifications are recommended
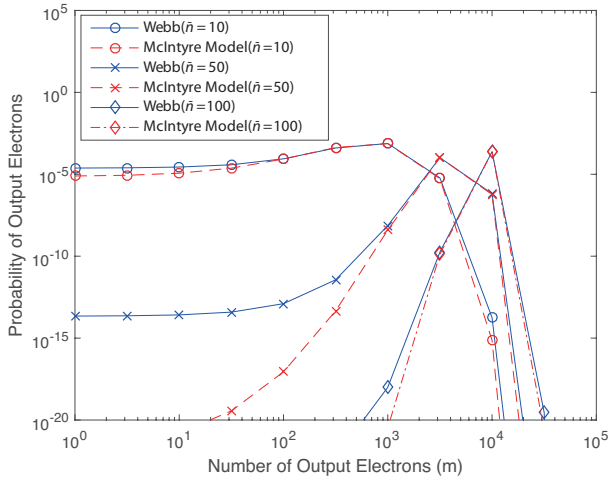
Fig. 3. APD electron output probability density functions based on the Webb and McIntyre models.

Fig. 4. Echo pulse width versus surface slope.

for the LALE to ensure successful scientific missions with respect to polar orbits at altitudes of 100 km or lower. Furthermore, these specifications help to achieve significant improvements when compared with previous altimetry data sets. They also ensure more consistent results between sunlight and shadow as well as laser pulse energy ≥ 2 mJ, beam divergence ≤ 100 μrad, repetition rate ≥ 16 Hz, and receiving telescope diameter ≥ 14 cm. Laser pulse energy plays an important role in the design of the laser altimeter because it is significantly related to performance, total mass, and the power budget of the lunar orbiter. Hence, minimum pulse energy is estimated to meet performance requirements of detection probability (P_D ≥ 0.95) and range error (ΔR ≥ 5 m) under the following conditions:

- An orbit altitude ranging from 70 km to 130 km
- A receiving telescope diameter of 14 cm
- A maximum surface slope of 45° and roughness variance of 4 m
- A false alarm probability equal to 0.001
- Daytime operations

The performance of the proposed laser altimeter is analyzed based on laser pulse energy under the above-mentioned conditions. It is assumed that laser altimetry is obtained by nadir pointing (ϕ=0) of the lunar orbiter. The following parameters are considered for numerical simulation: lunar surface albedo ρ=0.12 and solar spectral irradiance at Moon I_{sun}=0.65 W/m²/nm. Additionally, the ideal case wherein the low-pass filter impulse width is always equal to the echo pulse width, i.e., $\tau=\sigma_p$, is also considered.

Fig. 3 provides the comparison analysis between the Webb and McIntyre models to verify the application validity of the Webb model in the regions of signal and noise photons.
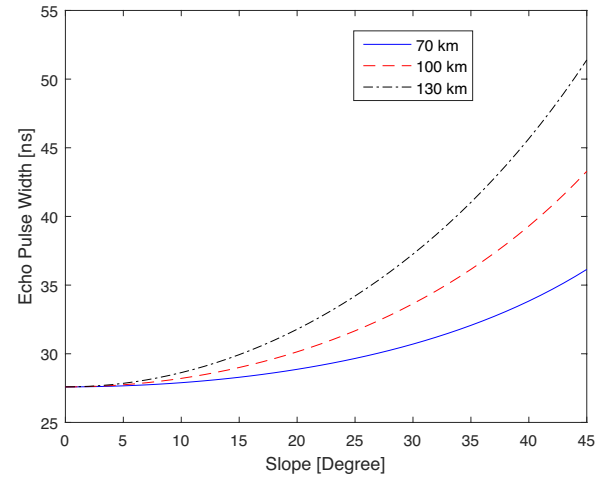
As observed in the figure, there is evident agreement in the region near the peak. Furthermore, the region of high output electrons indicates best agreement between the models. This agreement suggests that the Webb model can be applied to the calculation of detection and false alarm probabilities instead of the McIntyre model. Fig. 4 shows the echo pulse width versus surface slope for three orbiter altitudes, namely 70 km, 100 km, and 130 km. This is broadened due to factors including surface roughness, surface slope, laser beam divergence, and range to lunar surface when compared with that of the transmitted pulse width. Fig. 5 shows the average number of signal and noise photons as described in Eqs. (1) and (2) with respect to transmitted laser energy (3 mJ and 3.5 mJ) and slopes (30° and 45°), where the number of signal photons ranges from 50 to 400, and the number of noise photons ranges from 10 and 20. As shown in Fig. 6, the detection probability exceeds 93 % for the conditions of E_T=3 mJ and S=45°, and exceeds 98 % for the conditions of E_T=3 mJ and S=45°. It should be noted that the detection threshold level is adjusted to maintain a false alarm probability under 0.1 %. Given the results in Fig. 6, minimum laser pulse energy of 3.5 mJ satisfies the LALE performance requirement of detection probability, P_D≥0.95 even under harsh conditions of 130 km altitude, 45° slope, and daylight operation. Fig. 7 shows the results of SNR and range error as a function of altitude for the selected transmitted laser pulse energy (3.5 mJ) and slopes (30° and 45°) to verify the performance requirements of range error related to SNR. Additionally, by accounting for the range error analysis in Fig. 7, the LALE requirement on range error or uncertainty is also satisfied with respect to the transmitted laser pulse energy of 3.5 mJ for a surface slope less than 45°. In order to illustrate the detailed understanding of the relations between the laser pulse energy
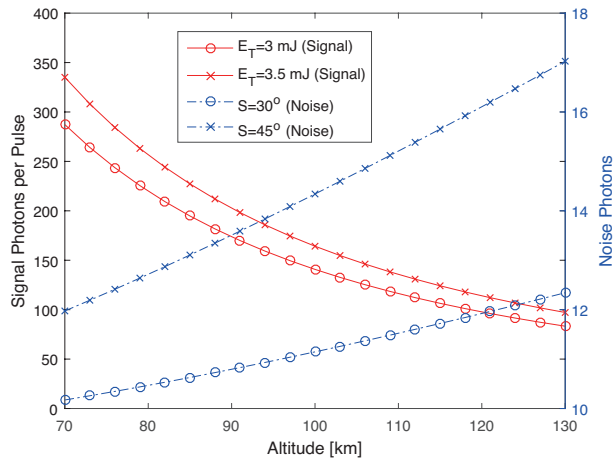
Fig. 5. Average signal and noise photons in daylight operation for receiving a telescope diameter of 14 cm.
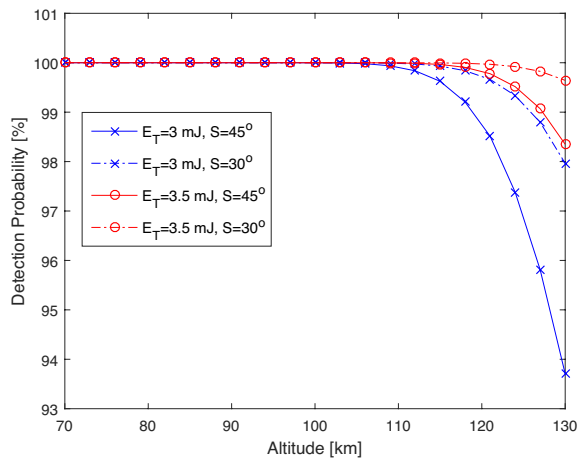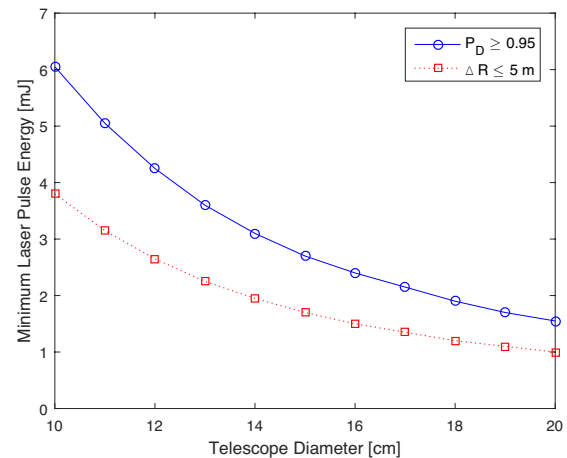

Fig. 6. Daylight detection probability for receiving a telescope diameter of 14 cm.
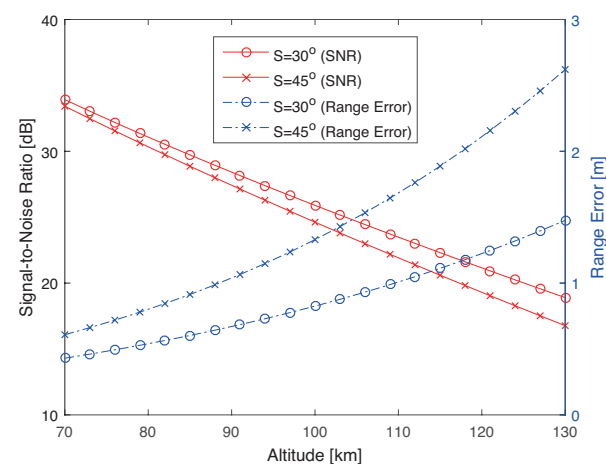
Fig. 7. Signal-to-noise ratio and range error in daylight operation for receiving a telescope diameter of 14 cm and a transmitted laser pulse energy of 3.5 mJ.

and receiving telescope diameter, Fig. 8 shows the minimum laser pulse energy as function of telescope diameter to meet

Fig. 8. Minimum laser pulse energy versus telescope diameter to meet the performance requirements of detection probability ($P_D \geq 0.95$) and range error ($\Delta R \geq 5$ m) under conditions involving an altitude of 130 km and a surface slope of 45°.

the performance requirements of detection probability ($P_D \geq 0.95$) and range error ($\Delta R \geq 5$ m) under conditions of an altitude of 130 km and a surface slope of 45°. In practice, both laser pulse energy and telescope diameter are determined by considering the allocated resource budget for the laser altimeter including size, mass, power, and performance requirements.

5. CONCLUSIONS

In this study, a laser altimeter is proposed as an instrument candidate for the Korean lunar orbiter to provide the global topography of the Moon's surface and a better understanding of the gravitational field, and to support the scientific mission of other payloads. The orbiter is assumed to have a near-circular polar orbit with an altitude ranging from 70 km to 130 km. The study addressed LALE baseline design and analyzed LALE performance based on the Webb model through a numerical simulation involving detection probability, SNR, and range error. The LALE is designed such that it is capable of measuring distance, surface albedo, surface slope, and roughness.

Design parameters including laser pulse energy are validated based on numerical simulations to meet the following performance requirements: ≥ 95 % for detection probability and ≤ 5 m for range error. Specifically, laser pulse energy is focused on performance analysis because it is significantly related to performance, total mass, and power budget. Surface physical characteristics such as surface slope and roughness broaden the echo pulse width when compared with the transmitted laser pulse width

such that they degrade LALE performance. Simulations that accounted for the echo pulse width in a design that includes a 3.5 mJ laser pulse energy indicate that the LALE meets performance requirements for detection probability and range error under harsh conditions of 130 km altitude, 45° surface slope, and daylight operation.

ACKNOWLEDGMENTS

REFERENCES

Abshire JB, Sun X, Afzal RS, Mars orbiter laser altimeter: receiver model and performance analysis. Appl. Opt. 39, 2449-2460 (2000). http://dx.doi.org/10.1364/AO.39.002449

Bufton JL, Laser altimetry measurements from aircraft and spacecraft, Proc. IEEE 77, 463-477 (1989). http://dx.doi.org/10.1109/5.24131

Conradi J, The distribution of gains in uniformly multiplying avalanche photodiodes: experimental, IEEE Trans. Electron Devices 19, 713-718 (1972). http://dx.doi.org/10.1109/T-ED.1972.17486

Gardner CS, Ranging performance of satellite laser altimeters, IEEE Trans. Geosci. Remote Sens. 30, 1061-1072 (1992). http://dx.doi.org/10.1109/36.175341

Gunderson K, Thomas N, Rohner M, A laser altimeter performance model and its application to BELA, IEEE Trans. Geosci. Remote Sens. 44, 3308-3319 (2006). http://dx.doi.org/10.1109/TGRS.2006.880623

McIntyre RJ, The distribution of gains in uniformly multiplying avalanche photodiodes: therory, IEEE Trans. Electron Devices 19, 703-713 (1972). http://dx.doi.org/10.1109/T-ED.1972.17485

Riris H, Cavanaugh J, Sun X, Liiva P, Rodriguez M, et al., The lunar orbiter laser altimeter (LOLA) on NASA's lunar reconnaissance orbiter (LRO) mission, Proceedings of the ICSO 2010, Rhodes, Greece, 4-8 October 2010.

Santovito MR, Tommasi L, Sgarzi G, Romoli A, Mattei S, et al., A laser altimeter for BepiColombo mission: Instrument design and performance model, Planet. Space Sci. 54, 645-660 (2006). http://dx.doi.org/10.1016/j.pss.2006.03.003

Sun X, Davidson FM, Boutsikaris L, Abshire JB, Receiver characteristics of laser altimeters with avalanche photodiodes. IEEE Trans. Aerosp. Electron. Syst. 28, 268-275 (1992). http://dx.doi.org/10.1109/7.135452

Thomas N, Spohn T, Barriot JP, Benz W, Beutler G, et al., The BepiColombo laser altimeter (BELA): concept and baseline design, Planet. Space Sci. 55, 1398-1413 (2007). http://dx.doi.org/ 10.1016/j.pss.2007.03.003

Wang J, Shu R, Chen W, Jia J, Wang B, et al., Laser altimeter of CE-1 payloads system, Sci. China Phys. Mech. Astron. 53, 1914-1920 (2010). http://dx.doi.org/ 10.1007/s11433-010-4085-z

Webb PP, McIntyre RJ, Conradi J, Properties of avalanche photodiodes, RCA Rev. 3, 234-278 (1974).